RSC Advances

PAPER

View Article Online
View Journal | View Issue



Cite this: *RSC Adv.*, 2025, **15**, 48149

# Precise dopant detection and transport properties of boron ion-implanted silicon solar cells

Monika Verma, [ab] Sanjeev Gautam, *[b] Bibek Ranjan Satapathy, [c] Weon Cheol Lim, [d] Ram Charan Meena, [e] Devarani Devi, [e] Suvankar Chakraverty [c] and Keun Hwa Chae [d]

Silicon solar cells continue to dominate photovoltaic technology, holding a market value of ~98% with an efficiency of 13–24% at the commercial level, which is limited by the recombination process and generated defects during the fabrication process. This study presents p–n junction fabrication using the ion beam technology, where boron species are implanted at a low energy of 35 keV into n-type Si (100). Doping was confirmed by X-ray photoelectron spectroscopy (XPS), which outperformed other conventional techniques (RBS and XRD) with exceptional elemental detection sensitivity. The shift in binding energy was observed to be 0.24 eV for the main peak in the silicon 2p spectra, resulting from the incorporation of boron into the silicon lattice. The local electronic environment modification was investigated by near-edge X-ray absorption fine structure (NEXAFS) spectroscopy at the O K-edge, which showed local hybridization consistent with boron incorporation and was also validated by FEFF simulations. Moreover, transport measurements exhibited diode-like *I–V* characteristics obtained using linear sweep voltammetry that were consistent with the Shockley diode model, indicating the formation of a p–n junction and notable suppression of the leakage current to 0.63 μA. Collectively, these findings evidence that the ion beam technology is a viable approach for the fabrication of reduced-defect structures, which are essential for the advancements of photovoltaics.

Received 6th September 2025
Accepted 18th November 2025

DOI: 10.1039/d5ra06708a

rsc.li/rsc-advances



## 1 Introduction

The growing global demand for sustainable and clean energy has revolutionized the renewable sources' share in power generation from 30% in 2023 to 46% by 2030, primarily driven by solar and wind energies. According to the International Energy Agency (IEA),[1] power generation from renewable energy sources is projected to rise by 90%, reaching approximately 17 000 TWh between 2023 and 2030. Crystalline polysilicon-based cells[2] account for over 98% of the total market share, surpassing other efficient cell designs like passivated emitter and rear cell (PERC) or TOPCon, heterojunction and back contacts. In spite of their prevalence, silicon solar cells have limited efficiency due to defects in their structure, promoting radiative and non-radiative recombination rates, Auger and surface recombination, Shockley-Read-Hall (SRH) recombination, and low lifetime of separated charge carriers.[3] Even a marginal increment in the lifespan of Si solar cells or an improvement in their efficiency can lead to significant global economic benefits by increasing productivity per unit of input.

Commercial procurable silicon solar cells are typically fabricated *via* thermal diffusion, plasma-enhanced fabrication, or RF sputtering techniques, which often introduce defects in the lattice of the solar cells.[4] These defects trap the photo-generated electron–hole pairs after the incidence of light, leading to the recombination of charge carriers and resulting in a decrease in the quantum efficiency of the cells.[5,6] To mitigate these effects, solar cell design should be incorporated with defect engineering strategies like (i) reducing the occurrence of defects, (ii) eliminating impurities from the active regions of the device or rearranging them into configurations that are less detrimental, and (iii) implementing defect passivation.[7] For defect-free structures, stability, and high-performance silicon solar cells, the ion beam technology offers a promising approach for the fabrication and modification of the silicon lattice.[8]

Ion beam implantation can be extensively used for the fabrication of p–n junctions by doping the ions into the host atom, providing a novel approach for next-generation solar cells.[9] This technology offers repeatability, reliability, and precision engineering for defect-minimized structures with enhanced transport properties. It involves the ions traveling

[a]*Energy Research Centre, Panjab University, Chandigarh 160014, India*
[b]*Advanced Functional Materials Lab, Dr S.S. Bhatnagar University Institute of Chemical Engineering & Technology, Panjab University, Chandigarh 160014, India. E-mail: sgautam@pu.ac.in; Tel: +91 97797 13212*
[c]*Institute of Nano Science and Technology, Mohali, Punjab 140306, India*
[d]*Advanced Analysis & Data Center, Korea Institute of Science and Technology, Seoul 02792, South Korea*
[e]*Inter-University Accelerator Centre, New Delhi 110067, India*

from the source materials through the beam line with defined energy and coming to rest beneath the surface of the substrate depending on their depth profile.[10,11] It has been employed for doping various ions in the production of ICs, like boron, phosphorus, arsenic, indium, antimony, nitrogen, and boron difluoride.[12] Ion beam-induced damage can be modeled using computational tools, such as SRIM/TRIM software, for the calculation of the range and transport mechanism into matter up to energies of 2 GeV amu$^{-1}$. It is created by Biersack, Ziegler, Littmark, *et al.*[13] and utilizes a Monte Carlo approach to predict the various parameters of ion–target interactions. These parameters include ion penetration depth, beam straggle, electronic and nuclear energy losses, energy deposition within the target material, phonon generation and its coupling with electrons, sputtering rates, vacancy concentration, displacement per atom (dpa), among others.[14,15] Research conducted by Mikoushkin *et al.*[16] investigated the implantation of nitrogen ions ($N_2^+$) in n-GaAs. It created a nitride nanolayer and formed a cluster of $GaAs_{1-x}N_x$, which was detected using the X-ray photoelectron spectroscopy (XPS) technique at a specific binding energy scan of N 1s. In a subsequent study, the same group[17] implanted the $N_2^+$ ion again at an energy of 1.5 keV. However, the detection of the fabricated layer was performed by high resolution XPS with synchrotron radiation. Their findings concluded that the primarily fabricated nitride layer had a wide band-gap (GaN) with the characteristics of quantum dots. Furthermore, the same group conducted another study,[18] with different $Ar^+$ ions at an energy of 1.25 keV ion irradiation for the conversion of conductivity from n to p-type GaAs, forming a p–n junction, studied using XPS. Additionally, Qahtan *et al.*[19] studied the production of oxygen vacancies in $TiO_2$ mesoporous films using $Ar^+$ ions at an energy of 500 eV. High resolution XPS confirmed the presence of oxygen, which was linked to lattice oxygen, oxygen vacancies, and absorbed oxygen.

In this study, a p–n junction was fabricated by implanting boron ions onto the upper layer of an n-type Si(100) substrate using ion beam implantations.[20] The depth penetration and doping density were precisely controlled by the energy and the fluence of the implantation, respectively,[21] enabling the formation of a uniform, defect-minimized layer for efficient electron–hole pair generation. Unlike conventional fabrication methods, here, employment of ion beam technique was particularly done for the effective doping of boron. Optimal doping at a certain fluence and energy is essential for a precise bandgap, and deviation from these parameters can enhance thermal fluctuations and increase the cell temperature.[22] Further, an excessive doping concentration can alter charge carrier dynamics by extending their mean free path, ultimately reducing carrier lifetime and negatively impacting quantum efficiency. Prior to evaluating the transport properties using the *I–V* characteristics of a fabricated p–n junction, it is essential to verify and ensure the doping of boron in Si(100). Moreover, X-ray diffraction (XRD), Rutherford backscattering spectrometry (RBS), and secondary ion mass spectrometry (SIMS) are well-established methods owing to their respective purposes but are unable to detect implanted ions.[23,24] However, X-ray photoelectron spectroscopy (XPS) plays an important role in surface analysis and in verifying the boron presence in the Si(100) lattice. It is a powerful technique for the detection of chemical bonds, charge states, and elemental compositions, which also provides some external information, like concentration, core-level lifetimes, multi-electron processes, and other phenomena, like Auger electron emissions, plasmons, and inelastic energy losses.[25,26] In addition, near-edge X-ray absorption fine structure (NEXAFS) spectroscopy was performed at the O K-edge to study the hybridization and to examine the changes in the local electronic environment after doping, along with the simulations using FEFF9.6, providing theoretical and physical aspects of hybridization effects.[27] The *I–V* measurements further validated the successful p–n junction formation with a significant reduction in leakage current, which can enhance the performance over conventionally fabricated solar cells.

## 2 Fabrications and characterization

### 2.1 Fabrication using ion implantations

Boron ions were implanted on a 1 × 1 cm$^2$ n-type Si(100) substrate using a low energy ion beam at an energy of 35 keV, considering three different fluences, 1 × 10$^{14}$, 1 × 10$^{15}$, and 1 × 10$^{16}$ ions per cm$^2$, using the KIST ion-beam facility.[28] Implantation of boron was performed at a beam current of 500 nA in an ultra high vacuum of 10$^{-9}$ mbar at room temperature. SRIM/TRIM software was used to calculate the stopping range, lateral ranges of the ions, and energy loss *via* phonons for an energy of 35 keV before implantation. The respective outcomes are shown in Fig. 1(a)–(c). Four different samples were named as nSi-P for pristine, BN1 for 1 × 10$^{14}$, BN2 for 1 × 10$^{15}$, and BN3 for 1 × 10$^{16}$. Before implantation, the wafers were cleaned using acetone and methanol for the removal of organic residues, followed by RCA cleaning using hydrogen peroxide: ammonium hydroxide: deionized water (DI) in a 1 : 1 : 5 ratio. The final step involved dipping the wafers in 2% diluted hydrofluoric acid for 2 minutes, followed by rinsing with DI and then blow-drying. During characterizations, each sample was chemically etched out for the removal of the surface $SiO_2$ layer with a solution of 5 ml of nitric acid (70%) and 3 ml of hydrofluoric acid (49%) after optimization based on the calculation of the etching rate and depth of deposition.

### 2.2 Characterizations

X-ray photoelectron spectroscopy (XPS) based on the photoelectric effect is pivotal for the analysis of deposited thin films

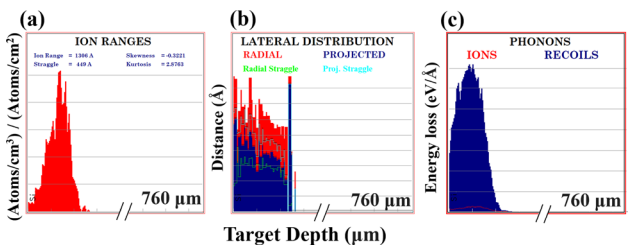


Fig. 1 SRIM/TRIM simulation for boron ions at an energy of 35 keV: (a) stopping range of ions, (b) lateral range of ions, and (c) energy loss *via* phonons.

by detecting the emission of photoelectrons. Mathematically, this can be written as eqn (1),[29] where the ejection of an electron from the core level in the continuum from the solids is only possible if the incident photon energy is greater than or equal to the work function of the surface (see Fig. S1 in the SI).

$$h\nu = \mathrm{BE} + \mathrm{KE} + \varphi, \quad (1)$$

where $h\nu$ is the photon's energy; BE is the binding energy of an electron, which is a materialistic property independent of X-ray; KE is the kinetic energy of the photoelectron; and $\varphi$ is the work function. Conventionally, XPS is a surface-sensitive technique that provides only 10 nm depth information in the perpendicular direction to the surface. Although beyond 10 nm, electron may be ejected, they are unable to reach the analysers due to the shielding of other energy levels.[25,30] XPS is a non-destructive approach that provides qualitative analysis, chemical state, and quantitative analysis with a small excitation diameter depending on the beam size. In principle, XPS can also provide the information about the electronic structure and the presented different chemical species on the top surface, chemical bonds, oxidation state, charge distribution, *etc.*, investigated through chemical shifts. It has diverse applications in polymers, biomaterials, energy storage and conversion materials, nanostructures, thin films, and semiconductors.[31]

Here, the XPS of the thin films was characterized using a Thermo Fisher Scientific K-Alpha spectrometer instrument at the Institute of Nano Science and Technology (INST), Mohali, India. The instrument consists of a monochromatic light source, which produces X-ray Al K$\alpha$, with an energy resolution of 0.5 eV and standardized using pure gold metal. The pass energy of the XPS was 200 eV, with a good balance between the signal intensity and high resolution.

Near-edge X-ray absorption fine structure (NEXAFS) spectroscopy was performed at the 10D (XAS KIST) beamline of the Pohang Accelerator Laboratory (Pohang, South Korea). NEXAFS data were recorded in total electron yield (TEY, surface mode),[32] and calibration of energy was performed through standards in the grating energy range with an energy resolution of 0.04 eV. Further, the data were normalized by subtracting the background and fitting the pre- and post-edge tails using Athena.[33] *I–V* characteristics were measured using PSTrace software from PalmSens instruments at IIT Jodhpur, India.

## 3 Computational details

The theoretical aspect of NEXAFS has been studied using FEFF version 9.6, which was developed by J.J. Rehr,[34] for the study of the electronic structure of the boron-implanted samples. This software includes cards like self-consistent potentials (SCFs), which provide information about the Fermi level, full-multiple scattering (FMS) for cluster radius, *etc.*, and programs that are applicable to a distinctive spectrum. It was employed to investigate the hybridization and quantify the cluster size under the influence of exchange potentials, FMS, amplitude reduction factors (SO2), and self-consistency loop with 25 iterations for potential calculations. SO2 quantifies the reduction in the transition amplitude due to the core hole creation that occurs during the X-ray absorption process. More details about the usage of different cards were provided by Gautam *et al.*[27]

## 4 Results and discussion

X-ray photoelectron spectroscopy (XPS), as a surface sensitive technique, is used to characterize the thin film *via* the detection of different elements (except hydrogen and helium) presented on the surface, which helps in determining the oxidation states, elemental compositions (reference data from NIST[35]), chemical shifts, and calibrated access to the binding energies.[36] The XPS survey illustrated in Fig. 2(a) of the Si 2p scan for the pristine sample nSi-P exhibits the binding energy of 99.19 eV at the $Si^0$ state (Si $2p_{3/2}$),[37] 99.79 eV belongs to $SiO_x$/Si with oxidation state varying from 0 to +4, here represented +2 oxidation state, and 102.11 eV for $Si^{+4}$ state of the $SiO_2$ compound. Besides, Fig. 2(b) depicts the XPS survey of boron implanted along with the pristine sample, labeling each peak. It is possible that the Si plasma loss feature for 2s and 2p falls around 167.9 eV and 184.5 eV, respectively, overlapping with the boron region due to the same binding energy, but a narrow scan and significant atomic concentration of boron verifies its presence. Before the narrow scan, calibration was performed with standards and referenced with carbon to correct the shifted binding energy. Further, to ensure that the carbon from the tape did not skew the interpretation of the sample's surface chemistry, all high-resolution spectra were carefully fitted after appropriate background subtraction.

Fitting of XPS spectra involves the proper background function for the modeling of inelastic electrons, followed by a peak fitting model using a suitable function to deconvolute the core-level spectrum into sub-peaks.[38] The backgrounds of Si 2p and O 1s were removed using Shirley[39] and B 1s using the Tougaard baseline treatment. In addition, the Voigt function (Gaussian + Lorentzian) was used for boron's peak fitting, and the Gaussian function was used for Si 2p and O 1s, keeping the FWHM fixed. An atomic concentration of boron was estimated[40] using eqn (2) considering the relative sensitivity factor (RSF) for boron 0.376, silicon 0.9, and oxygen 2.881, which is instrument dependent.

$$\text{Atomic conc.}(\%) = \frac{\frac{I_i}{\mathrm{SF}_i}}{\sum_n \frac{I_n}{\mathrm{SF}_n}} \times 100 \quad (2)$$

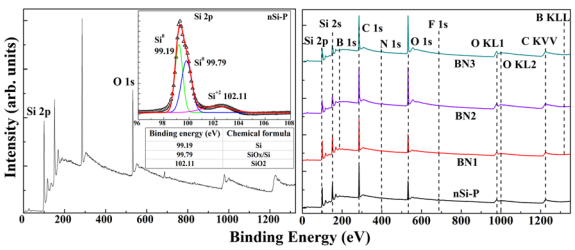


Fig. 2 X-ray photoelectron spectra of pristine sample nSi-P with Si 2p spectra (left), and boron implanted onto n-type Si, named as BN1, BN2, and BN3, with labeling of each corresponding peak (right ).

where $I_i$ is the integrated peak area for element i, and $\sum_n \frac{I_n}{SF_n}$ is for all $n$ elements presented in the sample. The surface atomic concentration of boron was evaluated as 6.23%, 18.40%, and 19.33% for BN1, BN2, and BN3, respectively. The abrupt changes in the atomic concentration for the sample BN2 having fluence of 10 times higher than BN1 is caused by the non-linear relationship between ion fluence and atomic concentrations. At lower fluence (BN1), the point defect has limited interaction, and above ($5 \times 10^{14}$ ions per $cm^2$), defect clusters start developing, which is attributed to sputtering effects and cascade overlap.[41] However, for BN3, the lattice reached a steady state of damage formation, leading to the formation of the cluster instead of the substitutional sites, as explained using the modified Kinchin–Pease equation.[42]

Fig. 3 illustrates the XPS spectra of doped samples BN1, BN2, and BN3 for the elements Si 2p, B 1s, and O 1s, respectively. As depicted in Fig. 3(a), the Si 2p spectrum assured the doping of boron with a shift towards higher binding energy at 102.75 eV with an oxidation state of $Si^{+4}$. As depicted in Fig. 3(b), B 1s spectra showed the doping of boron exhibiting different oxidation states $B^0$, $B^{+0.33}$, and $B^{+3}$ at 186.98 eV,[43] 189.42 eV,[44] and 192.06 eV[45] binding energy, respectively. The chemical states of boron corresponding to these binding energies were metallic, $B_6O$, and $B_2O_3$, making a composition with oxygen presented in the lattice of silicon[24,46] (and reference data taken from the NIST XPS database). The O 1s spectrum in Fig. 3(c) had the main peak at 531.95 eV, representing the presence of C=O, due to the contamination from carbon tape, and the deconvoluted peak at 532.07 eV demonstrates that the low binding energy component arises due to the absorption of $OH^-$.[47]

Besides, Fig. 3(d)–(f) depict Si 2p, B 1s, and O 1s scans of the BN2 sample ($1 \times 10^{15}$ at 35 keV), respectively. The Si 2p spectrum confirmed the doping of boron with a shift towards higher binding energy with oxidation state $Si^{+4}$ at 102.88 eV and verified the presence of $B_{15.9}Si_{19.0}O_{65.1}$.[48] After implantation, boron interacted with silicon in the matrix chemically and formed a bond with the oxidation states of $B^0$, $B^{+0.33}$, and $B^{+3}$. The deconvoluted peaks at binding energies[43] of 186.28 eV, 189.76 eV, and 192.9 eV were related to their existing composition in metal form, composition with oxygen,[44] silicon and boron,[48] respectively. Similarly, Fig. 3(f) shows the O 1s spectrum with binding energies of 532.14 eV and 532.72 eV.[49]

Fig. 3(g)–(i) illustrate the Si 2p, B 1s, and O 1s spectra of the BN3 sample ($1 \times 10^{16}$ at 35 keV), respectively. The implantation of boron into the lattice of silicon was very prominent that associates it, with different oxidation states of $B^0$ at binding energy[43] of 186.88 eV corresponds to metallic boron, $B^{+0.33}$ state at binding energy of 190.8 eV for $B_6O$,[44] and $B^{+3}$ at binding of energy 103.8 eV making a composition $B_{15.9}Si_{19.0}O_{65.1}$.[48] Fig. 3(g) and (i) confirm the doping of boron with shifting towards higher binding energy with oxidation state $Si^{+4}$ at 102.99 eV and verified the presence of $B_{15.9}Si_{19.0}O_{65.1}$.[48] As the fluence of boron increased, the binding energy shifted towards the higher ranges.[50] All the implanted samples had deviated binding energies, considering that the shielding effect (addition or removal of valence electrons), matrix interactions, and charging effects resulting from charge accumulation on the surface led to transient enhanced diffusion (TED). Interstitial atoms produced during implantation are responsible for this effect. Further, defects in the lattice, interstitial cluster, *etc.*, could trap or absorb these interstitially produced atoms.[51] The elements present in the silicon matrix interacted with each other chemically and electronically, changing their environment and causing a shift in the binding energy.

In addition to XPS, near-edge X-ray absorption fine structure (NEXAFS) spectroscopy at the O K-edge of pristine and BN3 was recorded, as depicted in Fig. 4(a). Since the surface of silicon is highly reactive to oxygen, it readily forms a native $SiO_2$ layer, which is removed using chemical etching. However, interfused oxygen (production of wafers) within the lattice of the fabricated samples provides valuable information about the hybridization of oxygen and the electronic modification of the respective doped elements in the implanted sample. The spectral features labeled $a_1$ and $a_2$ in Fig. 4(a) show the hybridization of the s orbital of oxygen with silicon atoms, where subsequent differences could be observed in the doped sample. The intense edge spectral features $a_3$ and $a_4$ were assigned to the hybridization

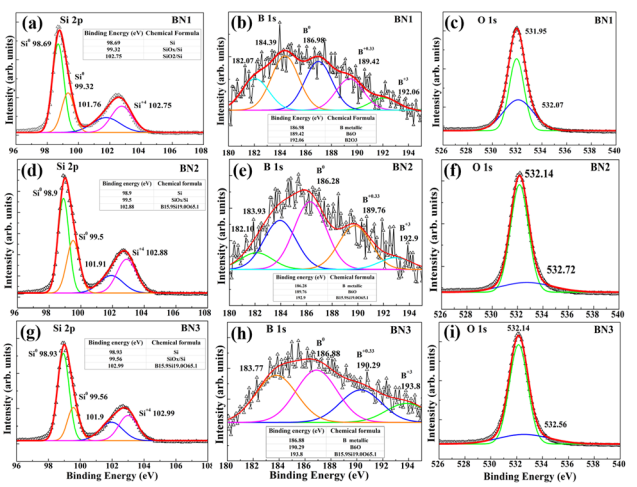


Fig. 3 X-ray photoelectron spectra of boron-implanted samples: (a)–(c) scan of Si 2p, B 1s, and O 1s, respectively, for BN1 ($1 \times 10^{14}$ at 35 keV); (d)–(f) scan of Si 2p, B 1s, and O 1s, respectively, for BN2 ($1 \times 10^{15}$ at 35 keV); and (g)–(i) scan of Si 2p, B 1s, and O 1s, respectively, for BN3 ($1 \times 10^{16}$ at 35 keV).

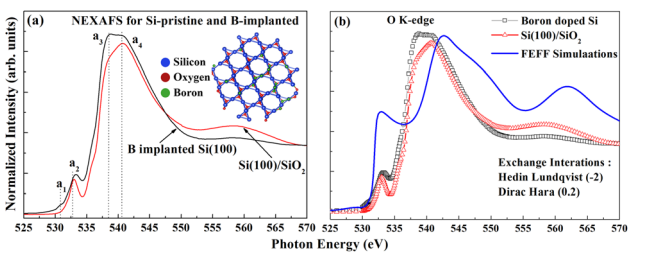


Fig. 4 Near-edge X-ray absorption fine structure spectra: (a) O K-edge of pristine and BN3, and (b) FEFF9.6 simulations, considering the exchange-correlation potential Hedin Lundqvist (HL) and Dirac Hara (DH) with no core hole.

between O 2p and Si 3p,[52] in which doping definitely disturbed the arrangements and respective hybridization. The distributions of energy in the implanted samples are clearly distinguishable from the pristine ones, indicating that the modification in the electronic structure resulted from the doping of boron. This suggests that boron implantation perturbed the Si–O bonds in the fabricated samples compared to pristine samples, affecting the spectral feature, which was in agreement with the XPS findings.

The obtained experimental spectra were also simulated using FEFF9.6, considering the exchange potential Hedin Lundqvist (HL) (−2 for the real part) and Dirac Hara (DH) (0.2 for the imaginary part) to account for the inelastic behavior of emitted photoelectrons and complex electron–electron interactions, respectively. The calculations were performed using 6 full multiple scattering (FMS) paths to determine the cluster size. However, larger FMS values could be used but showed negligible improvement over the chosen value. The reduction amplitude factor (SO2) that affected the amplitude of the absorption signal was restricted by many-body effects, which was set to 0.9, meaning a reduction of 10% signal, yielded the best fit to the experimental data, providing information about the local electronic environment. The self-consistent field was set to 3, with the local density of states varying from −20 (minimum energy) to 10 (maximum energy). The exchange potential for the fitting was HL, which was −2.0 in real parts, representing the increment in conduction area with relative molecular orbital ratios,[27] and DH was 0.2, as illustrated in Fig. 4(b).

Moreover, Fig. 5 depicts the diode-like *I–V* characteristics obtained using PSTrace software from PalmSens instruments. All the measurements were conducted at room temperature and under normal daylight without any particular light illumination using a tungsten probe. The data were recorded through linear sweep voltammetry, having a potential ranging from −2 V to 2 V, with a scan rate of 0.05 V $s^{-1}$ and step intervals of 0.05 V.

Fig. 5(a) illustrates the pristine sample, which exhibits a relatively high leakage current ($I_l$) of 1.5 μA compared to the implanted samples. Fig. 5(b) and (c) correspond to boron-implanted samples BN1 and BN2, showing the formation of a p–n junction,[53] where the relationship between current–voltage and the Shockley–diode equation is expressed as follows:

$$I = I_0(\exp^{(qV/\eta KT)} - 1),$$

where $I$ is the current, $I_0$ is the reverse saturation current, $q$ is the electronic charge, $V$ is the voltage, and $\eta$ is the ideality factor. At very low voltage ($V < 1$ V), the samples exhibit linear behavior, and the current grows exponentially at high voltages ($V > 1$ V).

The leakage currents 0.85 μA and 0.63 μA of BN1 and BN2, respectively, at −2 V are reduced in comparison to the pristine sample.[54] Interestingly, Fig. 5(d) reveals a distinct behavior for the sample implanted with a high fluence of $1 \times 10^{16}$ ions per $cm^2$, showing the reduction in knee voltage ($K_{knee}$). This demonstrated a sharp elevation in current and a leakage current of 1.57 μA, suggesting the possible formation of intermediate energy states within the material due to damage to the lattice. Another contributing factor could be TED caused by the supersaturation of silicon interstitial due to point defect.[55] Furthermore, this excess silicon interstitial generated, combined with boron doping, occupies the electrically inactive, metastable clusters, forming the mobile boron-interstitial pairs and subsequently large immobile clusters.[56,57] These findings demonstrate that precise and controlled doping *via* implantation significantly improves the *I–V* characteristics of the diode, making it a promising candidate for photovoltaic applications.

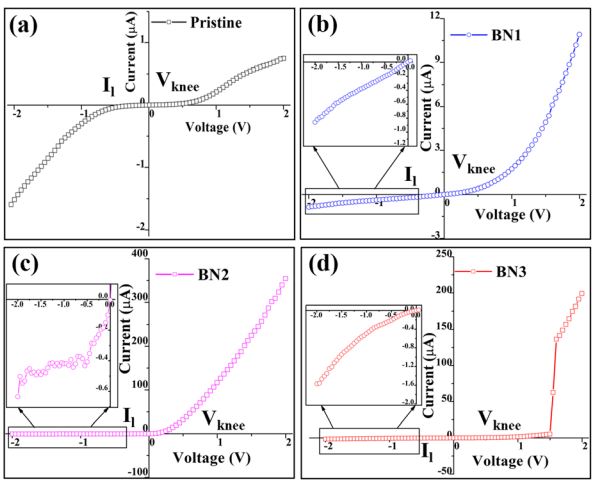


Fig. 5 Current–voltage characteristics of (a) pristine (nSi-P), (b) BN1, (c) BN2, and (d) BN3.

## 5 Conclusion

This study demonstrates the successful detection of dopants using X-ray photoelectron spectroscopy (XPS), a powerful surface-sensitive analytical technique. Boron was implanted into the n-type Si(100) for the fabrication of p–n junctions. XPS analysis revealed a shift in the binding energies of Si 2p and B 1s towards higher values, with the oxidation states, and confirmed boron incorporation. These shifts correspond to boron in multiple oxidation states $B^0$, $B^{+0.33}$, and $B^{+3}$, suggesting the formation of compounds with oxygen and silicon present in the lattice. The altered chemical and electronic environments induced by doping were responsible for the observed changes. Further, near-edge X-ray absorption fine structure (NEXAFS) spectroscopy supported the XPS results, showing changes in the O K-edge spectral features of the doped sample. These results were corroborated through simulations using FEFF9.6 to provide theoretical insight into the hybridization effects. Moreover, the *I–V* measurements revealed the formation of p–n junctions, which followed the Shockley diode equations that reduced the leakage current compared to the pristine sample while enhancing the forward current. Therefore, XPS emerges as a valuable tool for the successful detection of dopants in p–n junction formations *via* ion beam implantation, which is crucial for understanding junction behavior relevant to enhancing the efficiency of Si-based solar cells.

## Author contributions

Monika Verma: data curation, formal analysis, investigation, methodology, software, validation, writing – original draft; Sanjeev Gautam: conceptualization, formal analysis, funding acquisition, investigation, methodology, project administration, supervision, validation, visualization, writing – review & editing; Bibek R Satapathy, Weol-Cheol Lim, Ram Charan Meena, Devarani, Suvankar Chakraverty: data-curation; and Keun Hwa Chae: data-curation and software.

## Conflicts of interest

There are no conflicts to declare.

## Data availability

The data supporting this article have been included as part of the supplementary information (SI). Supplementary information: SRIM/TRIM, & FEFF, *etc.* See DOI: https://doi.org/10.1039/d5ra06708a.

## Acknowledgements

Authors acknowledges the research project from the University Grant Commission-Inter University Accelerator Center, New Delhi, India (UFR-73303) and Dr Ramcharan Meena (IUAC, New Delhi). Authors also acknowledge the research project under the DST INSPIRE Fellowships 2024 with Inspire code IF230126.

## Notes and references

1 I. Paris, Renewables 2024, 2024, https://www.iea.org/reports/renewables-2024/global-overview.
2 I. E. Agency, Innovation, 2024, https://www.iea.org/energy-system/renewables/solar-pv.
3 L. C. Andreani, A. Bozzola, P. Kowalczewski, M. Liscidini and L. Redorici, *Adv. Phys.:X*, 2019, **4**, 1548305.
4 K. Onishi, Y. Hara, T. Nishihara, H. Kanai, T. Kamioka, Y. Ohshita and A. Ogura, *Jpn. J. Appl. Phys.*, 2020, **59**, 071003.
5 T. Kamioka, Y. Isogai, Y. Hayashi, Y. Ohshita and A. Ogura, *AIP Adv.*, 2019, **9**, 10.
6 A. H. T. Le, V. A. Dao, D. P. Pham, S. Kim, S. Dutta, C. P. T. Nguyen, Y. Lee, Y. Kim and J. Yi, *Sol. Energy Mater. Sol. Cells*, 2019, **192**, 36–43.
7 B. L. Sopori, *Second Workshop: Role of Point Defects/Defect Complexes in Silicon Device Fabrication; Abstracts of Workshop Held 24-26 August 1992, Breckenridge, Colorado, National Renewable Energy Lab. (Nrel), Golden, Co (united states) Technical Report*, 1992.
8 Y.-W. Ok, A. D. Upadhyaya, Y. Tao, F. Zimbardi, K. Ryu, M.-H. Kang and A. Rohatgi, *Sol. Energy Mater. Sol. Cells*, 2014, **123**, 92–96.
9 M. Verma and S. Gautam, *Sustainable Energy Fuels*, 2025, 3202–3224.
10 Deepika and R. Kumar, *J. Electron. Mater.*, 2024, 1–15.
11 H. Thakur, P. Thakur, R. Kumar, N. B. Brookes, K. K. Sharma, A. P. Singh, Y. Kumar, S. Gautam and K. H. Chae, *Appl. Phys. Lett.*, 2011, **98**, 192512.
12 L. Rubin and J. Poate, *Ind. Phys.*, 2003, **9**, 12–15.
13 J. F. Ziegler and J. P. Biersack, in *Treatise on Heavy-Ion Science: Volume 6: Astrophysics, Chemistry, and Condensed Matter*, Springer, 1985, pp. 93–129.
14 U. Saha, K. Devan and S. Ganesan, *J. Nucl. Mater.*, 2018, **503**, 30–41.
15 R. E. Stoller, M. B. Toloczko, G. S. Was, A. G. Certain, S. Dwaraknath and F. A. Garner, *Nucl. Instrum. Methods Phys. Res., Sect. B*, 2013, **310**, 75–80.
16 V. Mikoushkin, Y. S. Gordeev, S. Y. Nikonov, A. Solonitsina, A. Zhuravleva and M. Brzhezinskaya, *Phys. Status Solidi C*, 2009, **6**, 2655–2657.
17 V. Mikoushkin, V. Bryzgalov, S. Y. Nikonov, A. Solonitsyna and M. Brzhezinskaya, *J. Surf. Invest.: X-Ray, Synchrotron Neutron Tech.*, 2012, **6**, 971–974.
18 V. Mikoushkin, E. Makarevskaya and M. Brzhezinskaya, *Appl. Surf. Sci.*, 2021, **539**, 148273.
19 T. F. Qahtan, T. O. Owolabi and T. A. Saleh, *J. Mol. Liq.*, 2024, **393**, 123556.
20 J. Krügener, E. Bugiel, H. J. Osten, R. Peibst, F. Kiefer, T. Ohrdes and R. Brendel, *20th International Conference on Ion Implantation Technology (IIT)*, 2014, pp. 1–4.
21 J. S. Williams and J. M. Poate, *Ion Implantation and Beam Processing*, Academic Press, 2014.
22 M. Wolf, *Sol. Cell.*, 1986, **17**, 53–63.
23 Y. Iijima and T. Tazawa, *Spectrochim. Acta B Atom Spectrosc.*, 2004, **59**, 1273–1276.
24 F.-Y. Lee, Z.-Z. Wu, L.-C. Kao, F.-M. Chang, S.-W. Chen, S.-K. JangJian, H.-Y. Cheng, W.-L. Chen, Y.-M. Chang and K. Y. Lo, *Sci. Rep.*, 2017, **7**, 13022.
25 F. A. Stevie and C. L. Donley, *J. Vac. Sci. Technol., A*, 2020, **38**, 6.
26 C. S. Fadley, *J. Electron Spectrosc. Relat. Phenom.*, 2010, **178**, 2–32.
27 S. Gautam, M. Verma, A. Thakur, J.-M. Chen and K. H. Chae, *J. Phys. D: Appl. Phys.*, 2025, **58**, 105308.
28 J. Kim, J. A. Eliades, B.-Y. Yu, W. C. Lim, K. H. Chae and J. Song, *Nucl. Instrum. Methods Phys. Res., Sect. B*, 2017, **391**, 57–63.
29 D. Li, Y. Chen, C. Zhou, C. Shi, Z. Xu, Z. Miao, Z. Xi and J. Han, *Mater. Chem. Front.*, 2024, 715–731.
30 C. J. Powell, *J. Vac. Sci. Technol. A*, 2020, **38**, 2.
31 D. Ketenoglu, *X-Ray Spectrom.*, 2022, **51**, 422–443.
32 M. Brzhezinskaya, I. V. Mishakov, Y. I. Bauman, Y. V. Shubin, T. A. Maksimova, V. O. Stoyanovskii, E. Y. Gerasimov and A. A. Vedyagin, *Appl. Surf. Sci.*, 2022, **590**, 153055.
33 B. Ravel and M. Newville, *Synchrotron Radiat. News*, 2005, **12**, 537–541.
34 J. J. Rehr, J. J. Kas, F. D. Vila, M. P. Prange and K. Jorissen, *Phys. Chem. Chem. Phys.*, 2010, **12**, 5503–5513.
35 A. V. Naumkin, A. Kraut-Vass and C. J. Powell, *NIST X-Ray Photoelectron Spectroscopy Database*, Measurement Services

Division of the National Institute of Standards and Technology (NIST) Technology Services, 2008.
36 G. Greczynski and L. Hultman, *Prog. Mater. Sci.*, 2020, **107**, 100591.
37 E. Puppin, I. Lindau and I. Abbati, *Solid State Comm.*, 1991, **77**, 983–986.
38 G. Greczynski and L. Hultman, *J. Appl. Phys.*, 2022, **132**, 011101.
39 M. Ishfaq, M. Rizwan Khan, M. Bhopal, F. Nasim, A. Ali, A. Bhatti, I. Ahmed, S. Bhardwaj and C. Cepek, *J. Appl. Phys.*, 2014, **115**, 17.
40 M. Xie, D. Li, L. Chen, F. Wang, X. Zhu and D. Yang, *Appl. Phys. Lett.*, 2013, **102**, 12.
41 M. A. Lively, B. Holybee, M. Toriyama, S. Facsko and J. P. Allain, *Sci. Rep.*, 2020, **10**, 8253.
42 S. Chen and D. Bernard, *Results Phys.*, 2020, **16**, 102835.
43 A. Burke, C. Brown, W. Bowling, J. Glaub, D. Kapsch, C. Love, R. Whitaker and W. Moddeman, *Surf. Interface Anal.*, 1988, **11**, 353–358.
44 M. Belyansky, M. Trenary and C. Ellison, *Surf. Sci. Spectra*, 1994, **3**, 147–150.
45 W. A. Brainard and D. R. Wheeler, *J. Vac. Sci. Technol.*, 1978, **15**, 1800–1805.
46 J. Yamauchi, Y. Yoshimoto and Y. Suwa, *Appl. Phys. Lett.*, 2011, **99**, 191901.
47 M. Naeem, S. Hasanain, M. Kobayashi, Y. Ishida, A. Fujimori, S. Buzby and S. I. Shah, *Nanotechnol.*, 2006, **17**, 2675.
48 L. Bois, P. L'Haridon, Y. Laurent, X. Gouin, P. Grange, J.-F. Létard, M. Birot, J.-P. Pillot and J. Dunoguès, *J. Alloys Compd.*, 1996, **232**, 244–253.
49 G. Hollinger, *Appl. Surf. Sci.*, 1981, **8**, 318–336.
50 K. Lee, C. Jo, D. Yoon, S. Baik and D.-H. Ko, *Appl. Surf. Sci.*, 2024, **657**, 159756.
51 M. Y. L. Jung, C. T. M. Kwok, R. D. Braatz and E. G. Seebauer, *J. Appl. Phys.*, 2005, **97**, 063520.
52 F. Frati, M. O. Hunault and F. M. De Groot, *Chem. Rev.*, 2020, **120**, 4056–4110.
53 V. Melnik, Y. Olikh, V. Popov, B. Romanyuk, Y. Goltvyanskii and A. Evtukh, *Mater. Sc. Eng. B*, 2005, **124**, 327–330.
54 J. A. Edmond, K. Das and R. F. Davis, *J. Appl. Phys.*, 1988, **63**, 922–929.
55 L. Pelaz, M. Jaraiz, G. H. Gilmer, H.-J. Gossmann, C. S. Rafferty, D. J. Eaglesham and J. M. Poate, *Appl. Phys. Lett.*, 1997, **70**, 2285–2287.
56 P. Stolk, H.-J. Gossmann, D. Eaglesham, D. Jacobson, C. Rafferty, G. Gilmer, M. Jaraiz, J. Poate, H. Luftman and T. Haynes, *J. Appl. Phys.*, 1997, **81**, 6031–6050.
57 C. J. Boyle, M. Upadhyaya, P. Wang, L. A. Renna, M. Lu-Díaz, S. Pyo Jeong, N. Hight-Huf, L. Korugic-Karasz, M. D. Barnes, Z. Aksamija, *et al.*, *Nat. Commun.*, 2019, **10**, 2827.